IEEE Access
Multidisciplinary | Rapid Review | Open Access Journal

Received 10 April 2024, accepted 2 May 2024, date of publication 9 May 2024, date of current version 17 May 2024.

Digital Object Identifier 10.1109/ACCESS.2024.3398786

RESEARCH ARTICLE

Impact of Speckle Deformability on Digital Imaging Correlation

JIAQIU WANG[1,2,3,*], HAO WU[4,*], ZHENGDUO ZHU[5], HUJIN XIE[2,3], HAN YU[2,3], QIUXIANG HUANG[2,3], YUQIAO XIANG[2,3], PHANI KUMARI PARITALA[3], JESSICA BENITEZ MENDIETA[2,3], HAVEENA ANBANANTHAN[2,3], JORGE ALBERTO AMAYA CATANO[2,3], RUNXIN FANG[6], LUPING WANG[4,7], AND ZHIYONG LI[2,3,4,8]

[1]School of Engineering, London South Bank University, SE1 0AA London, U.K.
[2]Centre for Biomedical Technologies, Queensland University of Technology, Brisbane, QLD 4000, Australia
[3]School of Mechanical, Medical and Process Engineering, Queensland University of Technology, Brisbane, QLD 4000, Australia
[4]School of Biological Science and Medical Engineering, Southeast University, Nanjing, Jiangsu 210096, China
[5]School of Computer Science, Queensland University of Technology, Brisbane, QLD 4000, Australia
[6]Jiangsu Institute of Metrology, Nanjing, Jiangsu 210023, China
[7]College of Mechanical and Electrical Engineering, China Jiliang University, Hangzhou, Zhejiang 310018, China
[8]Faculty of Sports Science, Ningbo University, Ningbo, Zhejiang 315211, China

Corresponding authors: Jiaqiu Wang (jiaqiu.wang@lsbu.ac.uk) and Zhiyong Li (zylicam@gmail.com)

The work of Jiaqiu Wang was supported in part by the Springboard Funding and the Global Collaboration Funding by London South Bank University; in part by the Early Career Researcher Grant by the Centre for Biomedical Technologies; and in part by the Roland Bishop Biomedical Engineering Research Award by Queensland University of Technology. The work of Zhiyong Li was supported in part by the Australian Research Council under Grant DP200103492; and in part by the National Natural Science Foundation of China under Grant 12172089, Grant 12372307, and Grant 61821002.

*Jiaqiu Wang and Hao Wu contributed equally to this work.

ABSTRACT Digital Image Correlation (DIC) has been widely used as a non-contact deformation measurement technique. Nevertheless, its accuracy is greatly affected by the speckle pattern on the specimen. To systematically evaluate how speckle deformability affects the precision of DIC algorithms. In this study, a test dataset of 2D speckle patterns with various prescribed deformation fields was numerically generated, containing two categories of speckles, i.e., the deformable and the non-deformable (rigid) ones. This dataset was used to evaluate the performance of inverse compositional Gauss-Newton (ICGN)-based DIC algorithms with two types of shape function (first-order and second-order), in the different scenarios of the deformation field. The results showed that imaging noise had a significant influence on the DIC algorithm. The first-order shape function (ICGN-1) performed better when tracking the simple linear deformation field. While the second-order shape function (ICGN-2) was proved to perform better on non-linear deformations. Moreover, the deformability of the speckle was found to have an obvious impact on the performance of the DIC algorithm. ICGN-2 could effectively reduce so-called speckle rigidity induced (SRI) error. Conclusively, ICGN-2 should be chosen as priority, because of its feasibility on non-linear deformation fields and speckle rigidity. While in the linear deformation scenarios, ICGN-1 was still a robust and efficient method.

INDEX TERMS Digital image correlation, speckle pattern, displacement measurement, motion tracking, imaging processing algorithms.

I. INTRODUCTION

Imaging-based deformation measurement technologies have been rapidly developed in recent years. The algorithms track the change of local pattern characteristics between adjacent frames and present the changes as displacement vectors. For example, digital image correlation (DIC) is a mature-developed algorithm for 2D full-field surface deformation measurement. It tracks the speckle pattern in pixel blocks to obtain the displacement vector field and strain map [1]. Based on the same principle, digital volume correlation (DVC) is developed to provide 3D full-field

The associate editor coordinating the review of this manuscript and approving it for publication was Byung-Gyu Kim.

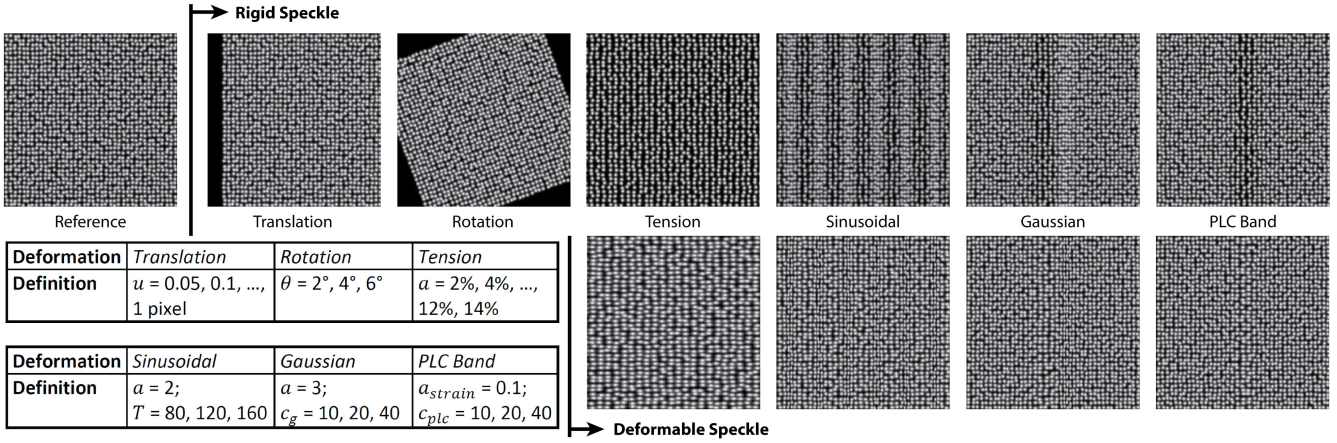

Deformation	*Translation*	*Rotation*	*Tension*
Definition	u = 0.05, 0.1, ..., 1 pixel	θ = 2°, 4°, 6°	a = 2%, 4%, ..., 12%, 14%

Deformation	*Sinusoidal*	*Gaussian*	*PLC Band*
Definition	a = 2; T = 80, 120, 160	a = 3; c_g = 10, 20, 40	a_{strain} = 0.1; c_{plc} = 10, 20, 40

FIGURE 1. Samples of the generated speckle pattern. The pattern at top left: the sample of the reference image. The six patterns at the top right: samples of rigid speckle patterns, the applied deformation fields. From left to right are pure translation and rotation tension, sinusoidal deformation, Gaussian deformation, and Portevin-Le Chatelier (PLC) band deformation. The chart at bottom left: the parameters used for generating the series of deformation of speckle patterns, whose mathematical definition could be found in Table 1. The four patterns at the bottom right: samples of deformable speckle patterns. From left to right, the applied deformation fields include tension, sinusoidal deformation, Gaussian deformation, and PLC band deformation.

volumetric displacement measurement [2], [3]. Compared to the experimental and the simulating approaches for strain analysis, the imaging-based measuring methods have the advantages of non-contact, harmless, high-precision, facticity and simple operability [4], [5], [6]. The sub-pixel registration algorithm is the key to determining the accuracy of DIC measurement. The original algorithm utilised in DIC was forward additive Newton-Raphson (FA-NR) algorithm, which was reported by Bruck et al. [7]. Subsequently, it has been continuously optimised to improve its accuracy and efficiency, and now it has been commonly used for accurate sub-pixel displacement measurement [8], [9], [10]. Nevertheless, as highlighted by several researchers, a significant limitation of the FA-NR algorithm is its huge computational cost [7], [11], [12]. In order to address the inherent redundancy in FA-NR calculations, an advanced inverse compositional Gauss-Newton (ICGN) algorithm was introduced and subsequently refined to be an efficient, robust, and accurate technology [13], [14]. Coupled with a robust reliability-guided tracking scheme, the ICGN algorithm has been anticipated to become a new standard approach in DIC. Indeed, since introduced, the ICGN algorithm has garnered widespread attention and acceptance [15], [16], [17], [18]. The above-mentioned methods have been widely used in engineering and especially in biomedical areas, where the scenarios strictly require non-invasive measurement. For example, Goh et al. [19] used the DIC method to measure the strain field of the large deformation materials like rubber. Lee and Ji [20] analysed the experimental data of polymer material under tensile loading using DVC technique. Li et al. employed the DVC algorithm in the mechanical test of soil [21], [22]. DVC-based deformation measurement has been reported to be applied on the magnetic resonance imaging (MRI) of intervertebral discs both *ex vivo* [23] and *in vivo* [24].

In the aforementioned DIC/DVC algorithms, the speckles play an important role in carrying the information of local displacement. These speckles in images could come from natural, for example, the sub-structure of the imaged tissue [24], specimen [25], and material [26]; or from artificial-manufacturing, such as painting [27] and adding tracing particles [28], [29]. Some previous research has discussed the quality of speckle patterns and investigated their influence on the DIC measurement errors. Lecompte et al. [30] presented a method for determining the speckle size distribution of speckle patterns using image morphology. Several parameters have been applied to evaluate the quality of speckle

TABLE 1. The definition of the deformation fields applied in this study. The principle of the generation of speckle patterns under various deformation fields was following the work of Su and Zhang [39]. In the rotated pattern, the deformation centre (x_0, y_0) was set at the centre of the speckle pattern (120, 120). In the deformed patterns with tension, Gaussian and PLC band, the deformation centre was set as x_0 = 120, i.e., the middle vertical line. In the sinusoidal deformation field, the phase b = 0. The definitions of other variables are listed in Figure 1.

Type	*Description*	*Denotation*
Translation	$u = u_0$	u: displacement; u_0: translation value.
Rotation	$\begin{bmatrix} x'-x_0 \\ y'-y_0 \end{bmatrix} = \begin{bmatrix} cos\,\theta & -sin\,\theta \\ sin\,\theta & cos\,\theta \end{bmatrix} \begin{bmatrix} x-x_0 \\ y-y_0 \end{bmatrix}$	(x, y): reference position; (x', y'): rotated position; (x_0, y_0): rotation centre; θ: rotation angle.
Tension	$u = a(x - x_0)$	a: amplitude of tension; $a > 0$: tension; $a < 0$: compression; x_0: deformation centre.
Sinusoidal	$u = a\,sin\left(\frac{2\pi x}{T} + b\right)$	a: amplitude of displacement; T: sinusoidal period; b: phase.
Gaussian	$u = a\,exp\left[-\frac{(x-x_0)^2}{c_g^2}\right]$	a: max amplitude of displacement; x_0: deformation centre; c_g: width of deformation.
PLC Band	$e_{xx} = a\,exp\left[-\frac{(x-x_0)^2}{c_{plc}^2}\right]$	e_{xx}: strain; a: max amplitude of strain; x_0: deformation centre; c_{plc}: width of deformation.

pattern, such as sum of square of subset intensity gradient (SSSIG) [31], [32], mean intensity gradient (MIG) [33], root-mean-square error (RMSE) [34] and E_f [35]. The concept entropy was also borrowed to quantify the speckle pattern quality [36], [37]. Atkinson et al. [38] recently reported a novel artificial neural network (ANN) to predict subset displacement error, such that the smallest subset size is appointed.

Specifically in acquired imaging data, these speckles can be separated into two categories, i.e. the deformable and the non-deformable speckles [40]. For instance, the painted pattern of speckles normally deformed following the deformation of the sample; while the added particles which are more rigid than the sample material intend not to deform, which might cause speckle rigidity induced (SRI) error [41], [42]. This study aims to systematically understand how the speckle deformability affects the precision of DIC algorithms. To achieve this, a test dataset of 2D speckle patterns with various deformation fields applied was numerically generated, which contained two versions corresponding to two categories of the deformable and the non-deformable (rigid) speckles. This dataset was used to evaluate the performance of the ICGN-based DIC algorithms, with first- and second-order shape functions, and in the different scenarios of the deformation field.

II. METHODS

This study used simulated speckle patterns with different deformation fields. As the generating process of 2D and 3D datasets shared the same principles, here to reduce the computational loads for the use of second-order shape function, 2D imaging datasets were selected in this study and the corresponding ICGN-based DIC algorithms with first- and second-order shape functions were employed.

A. SIMULATED SPECKLE PATTERN

The speckle patterns used in this study were generated using an in-house developed MATLAB (R2022a, MathWorks, Inc.) package. The definition of applied deformation fields on speckle patterns were based on the work of Su and Zhang [39]. The generated speckle patterns contained six types of deformation fields, including pure translation and rotation (for rigid speckles only), tension, sinusoidal, Gaussian, and Portevin-Le Chatelier (PLC) band deformation. Table 1 lists the theoretical definitions of each type of applied deformation field. Figure 1 presents the samples of generated speckle patterns with the aforementioned deformation fields.

In this algorithm, a set of Gaussian-shaped speckles with the aforementioned deformation fields applied were generated. It had the function to generate deformation fields with both deformable and rigid particles. To simulate the noise in the real image acquisition process, random Gaussian noise with the zero-mean value and different standard variances of 0, 5%, and 10% of the full 8-bit gray-scale were added to all of the images.

B. DIGITAL IMAGING CORRELATION ALGORITHM

ICGN-based DIC method was employed in this study, which was implemented based on an open-source library OpenCorr [43]. The DIC algorithm tracks each point of interest (POI) between the reference and the deformed image frames based on a defined-size subset, which is centred at the POI and contains a grid of pixels. The DIC algorithm first obtains the integer pixel displacement in each direction of the subset through fast Fourier transform-based cross-correlation (FFT-CC). Subsequently, it refines the displacement map to the sub-pixel level in the Gauss-Newton iteration. The DIC algorithm finally determines the best match of the target subsets in the deformed image to the reference subsets in the original image by calculating the correlation function between the reference and the target subsets, i.e., zero-normalized sum of squared differences (ZNSSD):

$$C_{ZNSSD}(\Delta\mathbf{p}) = \sum_{\xi} \left\{ \frac{f(\mathbf{x}+\mathbf{W}(\xi;\Delta\mathbf{p})) - f_m}{\sqrt{\sum_{\xi}[f(\mathbf{x}+\mathbf{W}(\xi;\Delta\mathbf{p})) - f_m]^2}} - \frac{g(\mathbf{x}+\mathbf{W}(\xi;\mathbf{p})) - g_m}{\sqrt{\sum_{\xi}[g(\mathbf{x}+\mathbf{W}(\xi;\mathbf{p})) - g_m]^2}} \right\}^2, \quad (1)$$

where $f(\mathbf{x})$ and $g(\mathbf{x})$ denote the pixel intensity at $\mathbf{x} = (x, y)^T$ in the reference and the target subsets; $\xi = (\Delta x, \Delta y, 1)^T$ is the local coordinates of integer pixels in the subset; f_m and g_m are the average intensities of the reference and the target subsets; $\mathbf{W}(\xi;\mathbf{p})$ represents the warp function, which describes the displacement and the deformation of the target subset relative to the reference subset; $\Delta\mathbf{p}$ represents the incremental deformation vector; and $\mathbf{W}(\xi;\Delta\mathbf{p})$ represents the incremental warp function exerted on the reference subset [13], [44].

The displacement between reference and target subsets are described using shape functions. Considering a POI $\mathbf{x} = (x, y)^T$ in the reference image, its corresponding point $\mathbf{x}' = (x', y')^T$ in the deformed image is described using shape functions:

$$\begin{bmatrix} x' \\ y' \end{bmatrix} = \begin{bmatrix} 1 & 0 & u \\ 0 & 1 & v \end{bmatrix} \begin{bmatrix} x \\ y \\ 1 \end{bmatrix}, \quad (2)$$

where u, v are the displacements of POI to be determined. The above shape functions is in zero-order, which can only describe the pure translation. The first-order shape function, which describes translation, rotation, shear and normal strains:

$$\begin{bmatrix} x' \\ y' \end{bmatrix} = \begin{bmatrix} 1+u_x & u_y & u \\ v_x & 1+v_y & v \end{bmatrix} \begin{bmatrix} x \\ y \\ 1 \end{bmatrix}, \quad (3)$$

where the u_x, u_y, v_x, v_y are the first-order gradient of u, v in the corresponding directions. The second-order shape

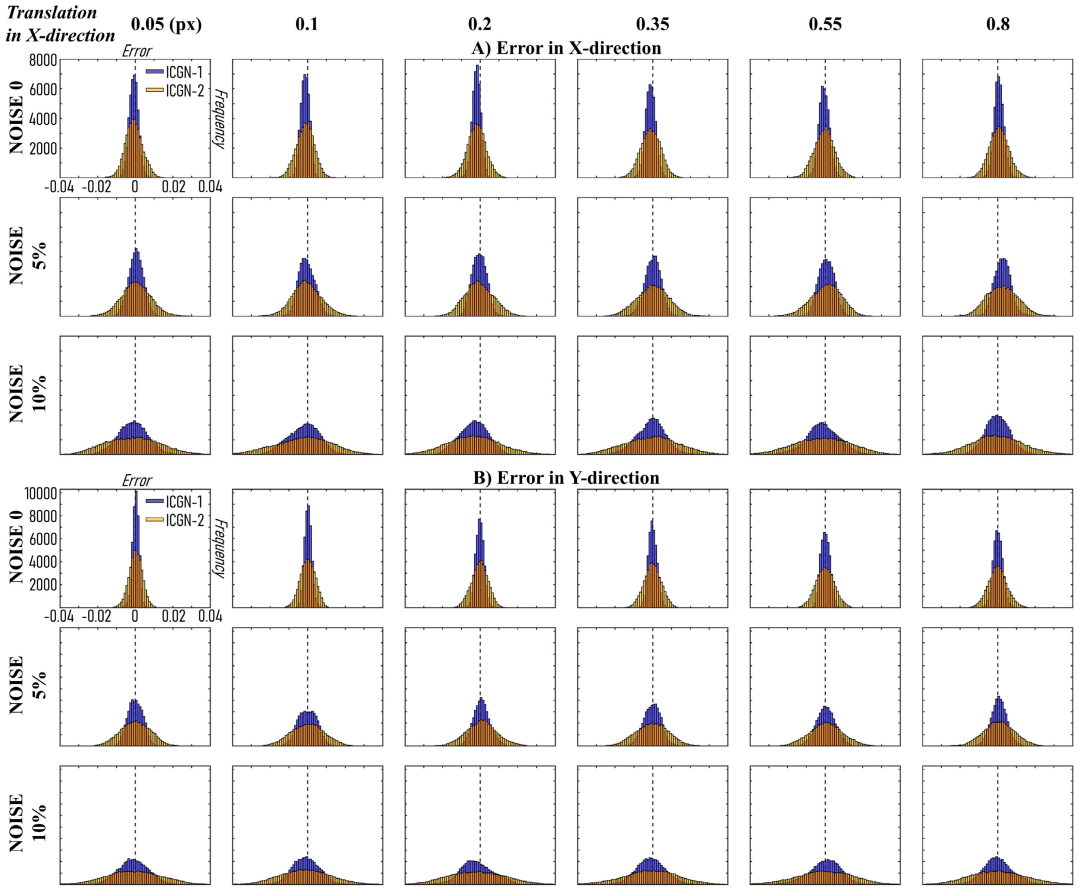

FIGURE 2. The histograms show the errors when using DIC to track the speckle patterns with pure translation applied in the x-axis direction (Part A: row 1-3) and in the y-axis direction (Part B: row 4-6). Each part, from left to right, shows the displacement applied in the x-direction by 0.05, 0.1 0.2, 0.35, 0.55, and 0.8 pixels. From top to bottom shows the three different noise variance levels 0, 5%, and 10%. In each subplot, the horizontal axis is the error in the x-direction between DIC-measured displacement (pixel) and the theoretical value; the vertical axis is the frequency, i.e., the count of points. The blue colour means the measurement by ICGN-1, while the yellow colour means ICGN-2. The axis ranges were unified into the same scale for each part.

function further includes the strain gradients and is able to describe complex deformation fields:

$$\begin{bmatrix} x' \\ y' \end{bmatrix} = \begin{bmatrix} \frac{1}{2}u_{xx} & u_{xy} & \frac{1}{2}u_{yy} & 1+u_x & u_y & u \\ \frac{1}{2}v_{xx} & v_{xy} & \frac{1}{2}v_{yy} & v_x & 1+v_y & v \end{bmatrix} \begin{bmatrix} x^2 \\ xy \\ y^2 \\ x \\ y \\ 1 \end{bmatrix}, \quad (4)$$

where $u_{xx}, u_{xy}, u_{yy}, v_{xx}, v_{xy}, v_{yy}$ are the second-order gradients of u, v [45].

C. ANALYSIS AND STATISTICS

All the deformed speckle patterns (with the resolution of 240 × 240 pixels) were calculated against to their initial status using ICGN-based DIC algorithms with the defined subset size of 31 pixels and grid step of 1. Both first- and second-order shape functions (hereinafter called the 'ICGN-1' and 'ICGN-2', respectively) were employed. The results between deformable versus rigid speckles, ICGN-1 versus ICGN-2, and different noise level were compared to each other.

III. RESULTS

A. TRANSLATION, ROTATION, AND TENSION

When the speckle pattern was given sub-pixel translation, the DIC-measured error distributions against the imposed value are presented in Figure 2. In general, DIC properly tracked the displacement in an acceptable and consistent error range with the translation steps increasing. The noise level and the order of shape function had a significant influence on the error distribution. The increased noise variance brought more errors in the displacement measurement. In both x-direction (same as the direction of applied displacement) and y-direction (without displacement loads, the error represented the systemic error of the DIC system), ICGN-1 had a narrower error distribution than ICGN-2.

Figure 3 plots the mean value and the standard deviation (SD) of the calculation error in the simple displacement fields of translation and rotation. The mean errors showed a

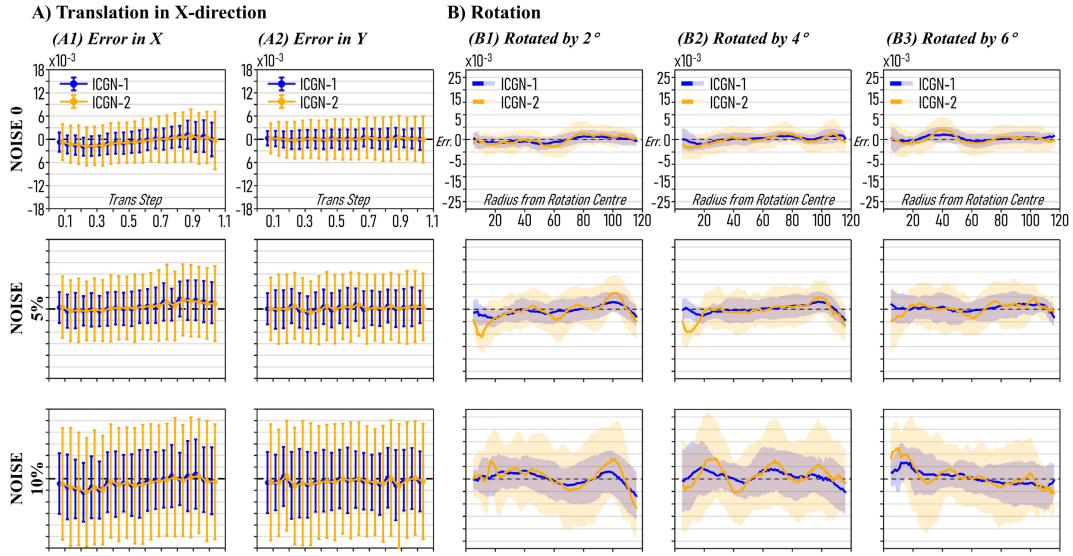

FIGURE 3. The mean value and standard deviation (SD) of calculation error plots show the DIC's performance when tracking the speckle patterns with pure translation and rotation. Part A presents the translation in the x-direction. The first column presents the error in the x-direction, while the second column shows that in the y-direction. Part B presents the rotation by 2°, 4°, and 6°, from left to right columns, respectively. Both Part A&B: from top to bottom rows shows the three different noise variance levels 0, 5%, and 10%. The blue colour means the measurement by ICGN-1, while the yellow colour means ICGN-2.

sinusoidal shape with period of one pixel and no dependency on the noise level and nor the shape function for translation. For noise level 0, the mean value of the calculation error for both shape function were almost the same. But the maximum SD error of ICGN-2 was 0.0075 pixels, which performed worse than the ICGN-1 (0.0044 pixels), because of the over-fitting problem in iteration process. With the increasing of noise level to 5% and 10%, the maximum SD of ICGN-2 increased to 0.0097 and 0.0155 pixels, respectively. Similarly, the maximum SD of ICGN-1 increased to 0.0054 and 0.0091. The same phenomenon of standard error was also observed in the y-direction. As no translation was added in the y-direction, therefore, it represented the system error of the DIC calculation. Regarding to the rotational displacement, the mean value and the SD error of both shape function were found oscillating with the increasing radius from rotation center and were irrespective of the rotate angle. The mean value and SD error of ICGN-2 in rotation were both larger than those of ICGN-1. The noise level was also found to have significant impact on the performance of calculation error.

A set of contour maps of the error between the imposed and calculated tension fields is plotted in Figure 4. With the tension magnitude increasing, the error pattern tended to oscillate at a higher frequency. The error of ICGN-1 was less than 0.01 pixels even when tension was increased to 14%, whereas the accuracy of the ICGN-2 was found to be worse (more than 0.02 pixels) for both rigid and deformable speckles. The error statistics of tension displacement fields are presented in Figure 5. When the magnitude of tension changed from 2% to 14%, the SD of ICGN-1 increased from 0.0031 to 0.0041 pixels for undeformable speckle patterns, while the SD of ICGN-2 raised significantly from 0.0057 to 0.0083 pixels. The deformable speckle patterns brought less mean errors, and the SD errors of both shape function maintained stable in a range of around 0.003 $\sim$ 0.005 pixels.

B. SINUSOIDAL, GAUSSIAN, AND PLC BAND DEFORMATION

Figure 6 plots both magnitude and error of the calculated sinusoidal-shape displacement field with a period of 80. Unlike the performance when tracking linear displacement field, ICGN-2 brought much smaller error than ICGN-1 in tracking the sinusoidal-shape deformation field with both rigid and deformable speckle patterns. Another interesting finding was that, although the magnitude of error was similar regardless of the speckle deformability, the error of deformable speckle varied smoothly, while the error of rigid speckle presented significant high-frequency oscillation, especially at the sections with large error magnitude. The displacement errors of sinusoidal-shape displacement field with different periods are shown in Figure 7. For such non-linear displacement field, the maximum measurement errors for all three period were less than 0.5, 0.2 and 0.15 pixels, respectively. Furthermore, the displacement errors were found increased following the frequency increasing for the sinusoidal deformation. The performance of ICGN-2 was found better than that of ICGN-1 in this non-linear deformation field. It was noted that high-frequency oscillatory errors were observed from the rigid speckle patterns.

More evidences of non-linear deformation fields of Gaussian and PLC-shaped displacement fields with different periods are shown in Figure 8. The period of applied

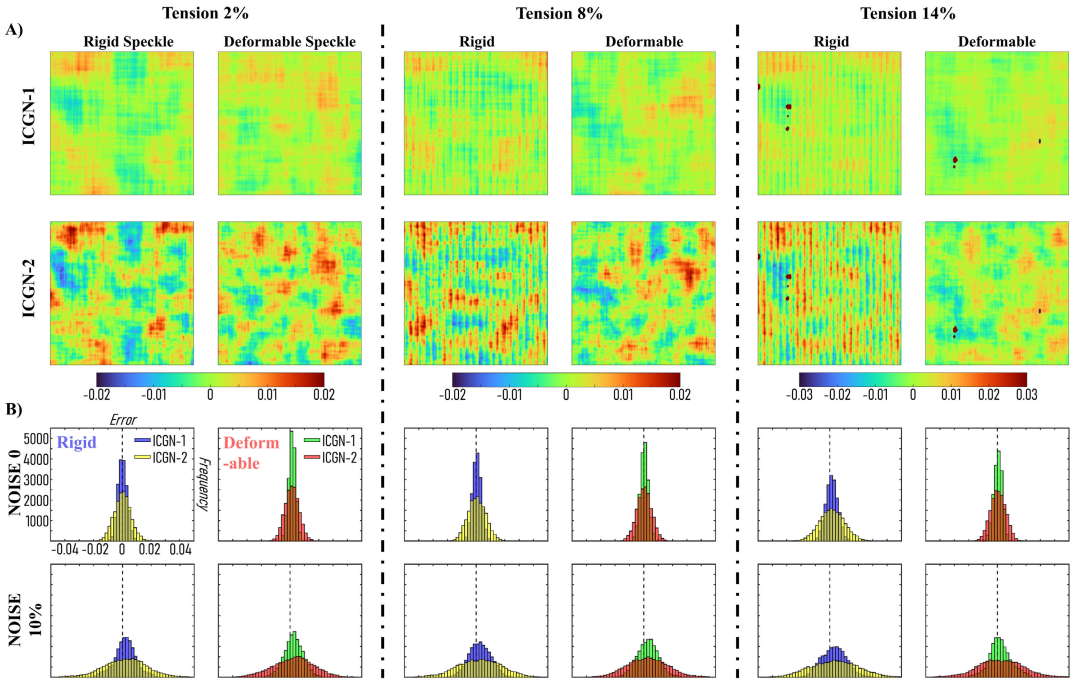

FIGURE 4. The results of tension with 2%, 8%, and 14% in x-direction. Part A: the contour plots of the error in the x-direction. In each subsection, the top row presents the results calculated using ICGN-1, bottom row presents that using ICGN-2. The left column represents the results calculated based on rigid speckle pattern, the right column represents that based on deformable speckle pattern. The shown contours were calculated using non-noise patterns. Part B: the histogram of the error in the x-direction. It presents the errors calculated based on speckle patterns with non-noise (top row) and 10% noise (bottom row). Left and right columns represent rigid and deformable speckle patterns, respectively.

displacement field, which represented the different displacement gradient, had significant influence on the error level. The errors of displacement for period 10 was larger than that of period 40 for both displacement fields. The improvement of using ICGN-2 and deformable speckle pattern were clearly indicated from these plots.

A Bland-Altman chart (Figure 9 and Table 2) was used to cross compare the aforementioned factors (the order of used shape function, speckle deformability, and period of displacement fields). The error level from ICGN-1 was found more sensitive to the sharpness of strain field, which indicated that the limitation of first-order shape function when tracking highly non-linear displacement fields.

IV. DISCUSSION

A. IMPACT OF NOISE

As a speckle pattern tracking algorithm, DIC is sensitive to noise level of the image data. Previous studies have proved that compared to the FA-NR algorithms. the ICGN algorithms had better performance on the elimination of noise-induced bias. This is because the higher-order Taylor expansion of gray-scale intensities caused by the deformation increment is performed on integer-pixel points [17], [46], [47].

Nevertheless, in this study, the noise level was found still to have a strong correlation to the DIC calculated error even with ICGN, irrespective of using ICGN-1/ICGN-2 and rigid/deformable speckle patterns. Therefore, to elevate the DIC accuracy further, the improvement of imaging quality and denoising would be one of the key priorities. Some pioneer studies demonstrated that appropriate pre-processing methods could enhance the image quality and reduce the noise level, hence, effectively mitigating DIC computational errors to some extent [48], [49], [50]. Inspired by the novel techniques in imaging processing [51], [52], [53] and noise-cancelling [54], [55], [56], the performance of DIC algorithms on image samples with pre-processing and denoising techniques will be further investigated in our future studies.

B. PARTICLE DEFORMABILITY AND ITS EFFECT

Particle pattern plays an important role in the DIC algorithms. Ideally the test sample used in DIC algorithms should have similar deformability for both speckle and the rest of areas, so that the tracked displacement and deformation of speckle structures could fully represent the deformation field of the testing sample. Nevertheless, in actual practical scenarios, the speckle deformability widely varies based on different methods of imposing speckles, such as natural-form sub-structures, spraying speckles, and mixing particles. In a deformed subset, the rigid speckles make the deformation matching more complicated, even when tracking simple deformation field, subsequently results in SRI error. To exhaust the potential of DIC, the deformable speckles are recommended to be chosen to use as far as possible, to reduce

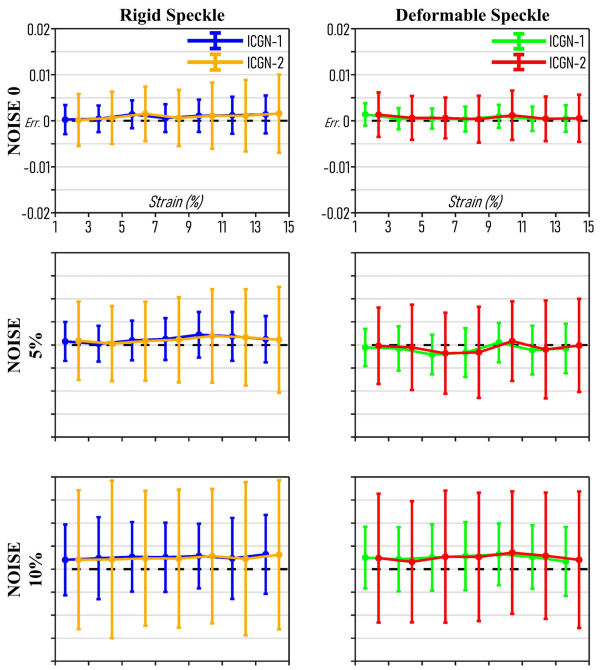

FIGURE 5. The error statistics of tension displacement fields from 2%, 4%,...,14%. From top to bottom rows, the results come from the speck patterns with noise levels of 0, 5%, and 10%. The left column shows the results of rigid speckle patterns, where the blue and yellow markers represent the calculation results from ICGN-1 and ICGN-2, respectively. The right column shows the results of deformable speckle patterns, where the green and red markers represent the calculation results from ICGN-1 and ICGN-2, respectively.

the magnitude and its oscillation of the error level. Also, the use of ICGN-2 has been proved could decrease the SRI error to some degree.

C. THE NATURE OF DEFORMATION FIELD

The nature of deformation field would be a decisive basis of choosing DIC-algorithms. Based on the results, ICGN-2 is not always a good option when tracking a simple and linear displacement field. In a linear displacement field, which could be ideally described by using first order shape foundation, the redundant second order factors from ICGN-2 algorithm causes over-fitting problem and induces larger error. In turn, in a complex displacement field, ICGN-1 performs worse than ICGN-2 due to missing of the second-order factors to describe the non-linear change of displacement field. The gradient of the non-linear displacement field is another key factor to determine the DIC performance. A sharp-changing displacement field (i.e., with large gradient) could significantly increase the error level expressly using ICGN-1. Contrastively, ICGN-2 could effectively track the high-gradient displacement field and reduce the error.

D. THE ORDER OF SHAPE FUNCTION

As introduced, there are various shape functions available in DIC. The zero-order shape function only describes the

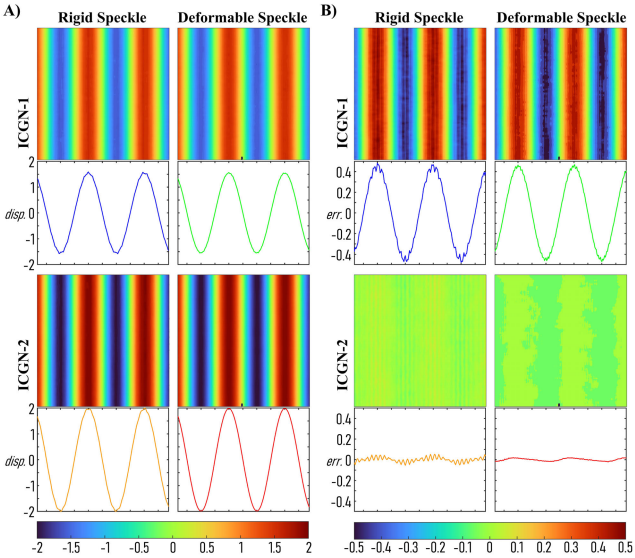

FIGURE 6. The DIC results of tracking the applied sinusoidal-shape displacement field with a period of 80: A) the calculated displacement field, and B) the error between calculated and applied displacement values. Each sub-figure contains four subplots, i.e., the ICGN-1 tracked rigid and deformable speck patterns (top row from left to right); and the ICGN-2 tracked rigid and deformable speck patterns (bottom row from left to right). Under each contour plot, a curve of displacement/error averaged from the pixels at each vertical line is plotted along with the horizontal axis, where the displacement gradient was applied.

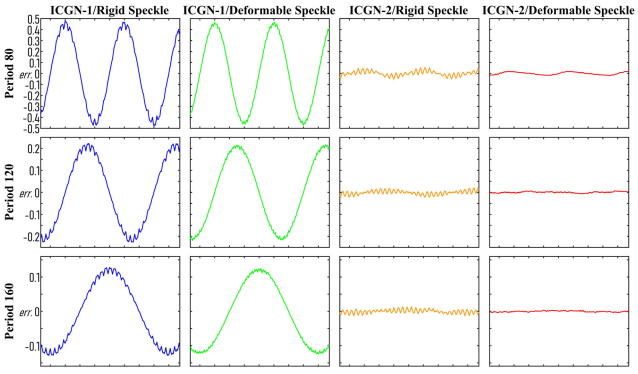

FIGURE 7. The errors of the DIC-tracked sinusoidal-shape displacement field with periods of 80, 120, and 160 (from top to bottom rows, respectively). From the left to right columns in sequence are ICGN-1 tracked rigid (blue) and deformable (green) speckle patterns, and ICGN-2 tracked rigid (yellow) and deformable (red) speckle patterns.

pure planer translational motions of subsets. It is mostly applied in theoretical studies and has limited applications in practical scenarios with large and non-linear deformation fields [31], [32], [57]. The first-order shape function used in ICGN-1 simplifies the subset deformation only consisting of translation, rotation and uniform strain. So that ICGN-1 is only suitable to describe such simple and linear deformation field. The second-order shape function used in ICGN-2 adds the second-order displacement gradient terms, which could describe the subset's non-linear deformation. Therefore, the accuracy of ICGN-2 is theoretically higher than the ICGN-1 algorithms when calculating non-linear

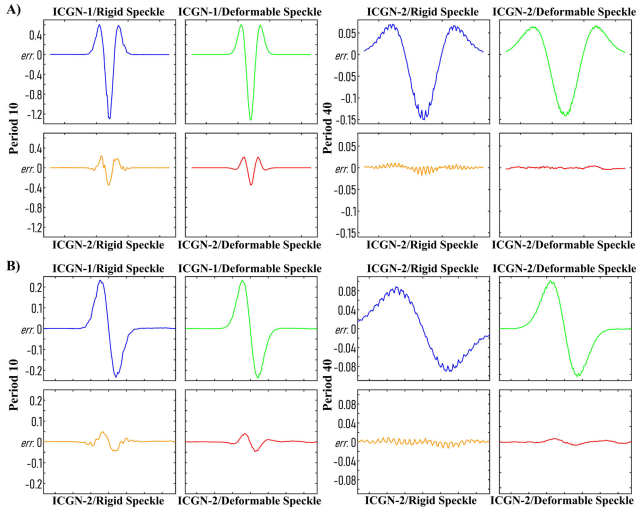

FIGURE 8. The errors of DIC-tracked (A) Gaussian and (B) PLC displacement field with periods of 10 (left) and 40 (right). Each subplot contains four curves, i.e., ICGN-1 tracked rigid (blue) and deformable (green) speckle patterns, and ICGN-2 tracked rigid (yellow) and deformable (red) speckle patterns.

TABLE 2. The parameters of mean, ±1.96SD of the corresponding Bland-Altman subplots in Figure 9.

A) Sinusoidal

Speckle Deformability	Period of Applied Displacement Field	Order of Shape Function	Parameters of Bland-Altman Plot MEAN	+1.96SD	-1.96SD
Rigid Speckle	*Period 80*	*ICGN-1*	-0.0046	0.6106	-0.6197
		ICGN-2	-0.0008	0.0465	-0.0481
	Period 120	*ICGN-1*	-0.0011	0.3037	-0.3059
		ICGN-2	0.0008	0.0234	-0.0218
	Period 160	*ICGN-1*	0.0176	0.1942	-0.1590
		ICGN-2	0.0004	0.0156	-0.0148
Deformable Speckle	*Period 80*	*ICGN-1*	-0.0047	0.6066	-0.6160
		ICGN-2	-0.0004	0.0252	-0.0261
	Period 120	*ICGN-1*	-0.0026	0.2960	-0.3011
		ICGN-2	-0.0006	0.0106	-0.0118
	Period 160	*ICGN-1*	0.0177	0.1924	-0.1571
		ICGN-2	0.0003	0.0103	-0.0097

B) Gaussian

Speckle Deformability	Period of Applied Displacement Field	Order of Shape Function	Parameters of Bland-Altman Plot MEAN	+1.96SD	-1.96SD
Rigid Speckle	*Period 10*	*ICGN-1*	-0.0056	0.6052	-0.6165
		ICGN-2	-0.0005	0.1607	-0.1616
	Period 20	*ICGN-1*	-0.0004	0.3196	-0.3204
		ICGN-2	0.0001	0.0340	-0.0337
	Period 40	*ICGN-1*	0.0004	0.1292	-0.1284
		ICGN-2	-0.0003	0.0126	-0.0132
Deformable Speckle	*Period 10*	*ICGN-1*	-0.0026	0.6274	-0.6325
		ICGN-2	-0.0003	0.1579	-0.1585
	Period 20	*ICGN-1*	-0.0005	0.3165	-0.3175
		ICGN-2	-0.0001	0.0242	-0.0243
	Period 40	*ICGN-1*	0.0009	0.1254	-0.1236
		ICGN-2	0.0002	0.0103	-0.0098

C) PLC

Speckle Deformability	Period of Applied Displacement Field	Order of Shape Function	Parameters of Bland-Altman Plot MEAN	+1.96SD	-1.96SD
Rigid Speckle	*Period 10*	*ICGN-1*	-0.0007	0.1690	-0.1704
		ICGN-2	-0.0007	0.0294	-0.0308
	Period 20	*ICGN-1*	0.0004	0.1491	-0.1483
		ICGN-2	0.0004	0.0142	-0.0133
	Period 40	*ICGN-1*	0.0007	0.1130	-0.1117
		ICGN-2	0.0005	0.0134	-0.0124
Deformable Speckle	*Period 10*	*ICGN-1*	0.0003	0.1695	-0.1689
		ICGN-2	0.0003	0.0273	-0.0267
	Period 20	*ICGN-1*	0.0004	0.1484	-0.1477
		ICGN-2	0.0004	0.0126	-0.0117
	Period 40	*ICGN-1*	0.0005	0.1106	-0.1097
		ICGN-2	0.0003	0.0099	-0.0093

deformation fields (i.e., sinusoidal, Gaussian and PLC band in this study). Nevertheless in the simple deformation fields (i.e., translation, rotation and tension in this study), the

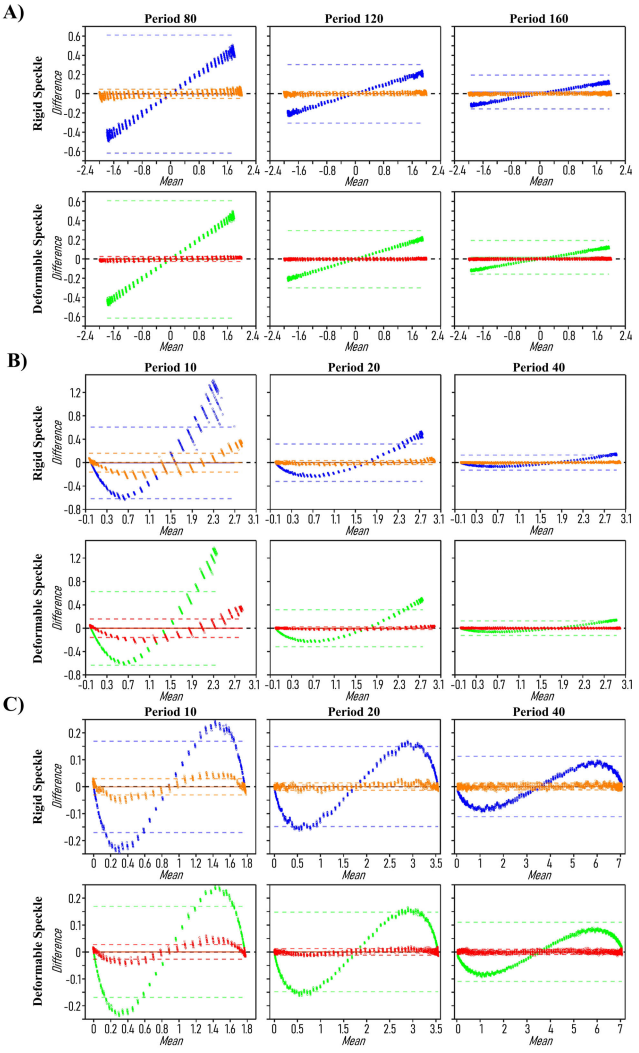

FIGURE 9. The Bland-Altman plots present the consistency of DIC-tracked displacement against the prescribed displacement: A) the sinusoidal-shape displacement; B) the Gaussian displacement; C) the PLC displacement. Each subplot contains three displacement field periods. And four colour labels were used to distinguish the shape function order and the speckle deformability: i.e., ICGN-1 tracked rigid (blue) and deformable (green) speckle patterns, and ICGN-2 tracked rigid (yellow) and deformable (red) speckle patterns. The parameters of mean, ±1.96SD of the each Bland-Altman subplot are listed in Table 2.

computation errors associated with a second-order shape function has been proved obviously larger than that with first-order shape function, because the redundancy high order terms (i.e., u_xx, u_xy, u_xx, v_xx, v_xy, v_yy, whose value should be zero in these simple deformation fields) of the second-order shape function are over-fitted with small non-zero values during the iterative process. This error in ICGN-2 could be compressed by using a larger subset.

Considering the majority of the practical applications of DIC/DVC algorithm are tracking complex and non-linear displacement field, also, the ability of reduce the SRI error, the second-order shape function-based ICGN-2 should be the preferred algorithm for DIC analysis. Whereas, the ICGN-1's advantages include fast processing time, low request of

computational resources, and stability when tracking linear deformation fields. It is still a robust choice if the deformation field is simple, linear, low gradient, and with deformable speckle patterns.

E. LIMITATIONS

This study used the simulated speckle patterns to analyse the DIC algorithms' performance. Limited by the used method of generating speckle patterns, besides the rotation, the deformation fields were only available to be loaded in single-axis direction. Thereby, this study did not include the complicated deformation field with bi-axis loads. Such as complex deformation field was expected to further highlight the advantages of using second-order shape function. In our next-step study, a finite element method (FEM)-based mesh method will be borrowed to generate the deformed images/speckle patterns with precise node-to-node displacement control, which could be used to test the DIC algorithms with more complex deformation fields.

The use of simulated speckle patterns in this study could eliminate potential errors from out-plane deformation, image acquisition quality and volume distortion during loading process. Nevertheless, it has to be noticed that the ideal rigid and deformed particles, and the ideal theoretical displacement fields like sinusoidal- and Gaussian- shapes were difficultly reproduced in the real experiment. Therefore, a validating experiment using real imaging data was not able to be included in this study. In the future, the deformation fields will be mimicked using our developed optical coherence tomography (OCT)-based mechanical test experiment [29]. Then the ICGN-1 and ICGN-2 based DVC algorithms will be able to be analysed based on the real experimental data.

V. CONCLUSION

This research utilised the simulated speckle patterns with various deformation fields, and investigated the performance of DIC algorithms in tracking deformation. The factors discussed in this study included the type of prescribed deformation fields, speckle deformability, imaging noise level, and the order of shape function. The imaging noise had significant influence on the DIC analytical results. ICGN-1 performed better when tracking simple linear deformation field. In turn, ICGN-2 was proved to have better performance on non-linear deformations. The deformability of speckle was found to have an impact on the performance of DIC algorithm, and the use of second order shape function could effectively reduce such SRI error. In the cases of complex deformation, the ICGN-2 could be chose as priority, because of its feasibility on non-linear deformation fields and speckle rigidity. However, in the sample cases, the ICGN-1 is still an robust and efficient method.

DECLARATION OF COMPETING INTEREST

The authors declare that they have no known competing financial interests or personal relationships that could have appeared to influence the work reported in this article.

REFERENCES

[1] N. McCormick and J. Lord, "Digital image correlation," *Mater. Today*, vol. 13, no. 12, pp. 52–54, Dec. 2010.
[2] B. K. Bay, "Methods and applications of digital volume correlation," *J. Strain Anal. Eng. Des.*, vol. 43, no. 8, pp. 745–760, Aug. 2008.
[3] A. Buljac, C. Jailin, A. Mendoza, J. Neggers, T. Taillandier-Thomas, A. Bouterf, B. Smaniotto, F. Hild, and S. Roux, "Digital volume correlation: Review of progress and challenges," *Experim. Mech.*, vol. 58, no. 5, pp. 661–708, Jun. 2018.
[4] B. Pan, W. Dafang, and X. Yong, "Incremental calculation for large deformation measurement using reliability-guided digital image correlation," *Opt. Lasers Eng.*, vol. 50, no. 4, pp. 586–592, Apr. 2012.
[5] Z. Tang, J. Liang, Z. Xiao, and C. Guo, "Large deformation measurement scheme for 3D digital image correlation method," *Opt. Lasers Eng.*, vol. 50, no. 2, pp. 122–130, Feb. 2012.
[6] X. He, R. Zhou, Z. Liu, S. Yang, K. Chen, and L. Li, "Review of research progress and development trend of digital image correlation," *Multidiscipline Model. Mater. Struct.*, vol. 20, no. 1, pp. 81–114, Jan. 2024.
[7] H. A. Bruck, S. R. McNeill, M. A. Sutton, and W. H. Peters, "Digital image correlation using Newton–Raphson method of partial differential correction," *Experim. Mech.*, vol. 29, no. 3, pp. 261–267, Sep. 1989.
[8] G. Vendroux and W. G. Knauss, "Submicron deformation field measurements: Part 2. Improved digital image correlation," *Experim. Mech.*, vol. 38, no. 2, pp. 86–92, Jun. 1998.
[9] H. Lu and P. D. Cary, "Deformation measurements by digital image correlation: Implementation of a second-order displacement gradient," *Experim. Mech.*, vol. 40, no. 4, pp. 393–400, Dec. 2000.
[10] B. Pan, "Reliability-guided digital image correlation for image deformation measurement," *Appl. Opt.*, vol. 48, no. 8, pp. 1535–1542, 2009.
[11] P. Bing, X. Hui-Min, X. Bo-Qin, and D. Fu-Long, "Performance of sub-pixel registration algorithms in digital image correlation," *Meas. Sci. Technol.*, vol. 17, no. 6, pp. 1615–1621, Jun. 2006.
[12] B. Pan and K. Li, "A fast digital image correlation method for deformation measurement," *Opt. Lasers Eng.*, vol. 49, no. 7, pp. 841–847, Jul. 2011.
[13] B. Pan, K. Li, and W. Tong, "Fast, robust and accurate digital image correlation calculation without redundant computations," *Experim. Mech.*, vol. 53, no. 7, pp. 1277–1289, Sep. 2013.
[14] Z. Jiang, Q. Kemao, H. Miao, J. Yang, and L. Tang, "Path-independent digital image correlation with high accuracy, speed and robustness," *Opt. Lasers Eng.*, vol. 65, pp. 93–102, Feb. 2015.
[15] Y. Gao, T. Cheng, Y. Su, X. Xu, Y. Zhang, and Q. Zhang, "High-efficiency and high-accuracy digital image correlation for three-dimensional measurement," *Opt. Lasers Eng.*, vol. 65, pp. 73–80, Feb. 2015.
[16] B. Pan and L. Tian, "Superfast robust digital image correlation analysis with parallel computing," *Opt. Eng.*, vol. 54, no. 3, Mar. 2015, Art. no. 034106.
[17] X. Shao, X. Dai, and X. He, "Noise robustness and parallel computation of the inverse compositional Gauss–Newton algorithm in digital image correlation," *Opt. Lasers Eng.*, vol. 71, pp. 9–19, Aug. 2015.
[18] J. Blaber, B. Adair, and A. Antoniou, "Ncorr: Open-source 2D digital image correlation MATLAB software," *Experim. Mech.*, vol. 55, no. 6, pp. 1105–1122, Jul. 2015.
[19] C. P. Goh, H. Ismail, K. S. Yen, and M. M. Ratnam, "Single-step scanner-based digital image correlation (SB-DIC) method for large deformation mapping in rubber," *Opt. Lasers Eng.*, vol. 88, pp. 167–177, Jan. 2017.
[20] S. Lee and W. Ji, "DVC analysis of a polymer material subjected to tensile loading with synchrotron radiation tomography," *Polym. Test.*, vol. 81, Jan. 2020, Art. no. 106204.
[21] C. Li, L. Kong, R. Shu, R. An, and H. Jia, "Dynamic three-dimensional imaging and digital volume correlation analysis to quantify shear bands in grus," *Mech. Mater.*, vol. 151, Dec. 2020, Art. no. 103646.
[22] C. Li, L. Kong, and R. An, "Evolution of cracks in the shear bands of granite residual soil," *J. Rock Mech. Geotechnical Eng.*, vol. 14, no. 6, pp. 1956–1966, Dec. 2022.
[23] S. Tavana, J. N. Clark, J. Prior, N. Baxan, S. D. Masouros, N. Newell, and U. Hansen, "Quantifying deformations and strains in human intervertebral discs using digital volume correlation combined with MRI (DVC-MRI)," *J. Biomechanics*, vol. 102, Mar. 2020, Art. no. 109604.

[24] S. Tavana, J. N. Clark, N. Newell, J. D. Calder, and U. Hansen, "In vivo deformation and strain measurements in human bone using digital volume correlation (DVC) and 3T clinical MRI," *Materials*, vol. 13, no. 23, p. 5354, Nov. 2020.

[25] B. K. Bay, T. S. Smith, D. P. Fyhrie, and M. Saad, "Digital volume correlation: Three-dimensional strain mapping using X-ray tomography," *Experim. Mech.*, vol. 39, no. 3, pp. 217–226, Sep. 1999.

[26] A. Bartulovic, Z. Tomicevic, A. Bubalo, and F. Hild, "Assessment of DVC measurement uncertainty on glass fiber reinforced polymers with various fiber architectures," *Coupled Syst. Mech.*, vol. 11, no. 1, pp. 15–32, 2021.

[27] N. Bretagne, V. Valle, and J. C. Dupré, "Development of the marks tracking technique for strain field and volume variation measurements," *NDT E Int.*, vol. 38, no. 4, pp. 290–298, Jun. 2005.

[28] M. Razani, A. Mariampillai, C. Sun, T. W. H. Luk, V. X. D. Yang, and M. C. Kolios, "Feasibility of optical coherence elastography measurements of shear wave propagation in homogeneous tissue equivalent phantoms," *Biomed. Opt. Exp.*, vol. 3, no. 5, p. 972, 2012.

[29] H. Wu, J. Wang, J. A. Amaya Catano, C. Sun, and Z. Li, "Optical coherence elastography based on inverse compositional Gauss–Newton digital volume correlation with second-order shape function," *Opt. Exp.*, vol. 30, no. 23, p. 41954, 2022.

[30] D. Lecompte, A. Smits, S. Bossuyt, H. Sol, J. Vantomme, D. Van Hemelrijck, and A. M. Habraken, "Quality assessment of speckle patterns for digital image correlation," *Opt. Lasers Eng.*, vol. 44, no. 11, pp. 1132–1145, Nov. 2006.

[31] Z. Y. Wang, H. Q. Li, J. W. Tong, and J. T. Ruan, "Statistical analysis of the effect of intensity pattern noise on the displacement measurement precision of digital image correlation using self-correlated images," *Experim. Mech.*, vol. 47, no. 5, pp. 701–707, Sep. 2007.

[32] B. Pan, H. Xie, Z. Wang, K. Qian, and Z. Wang, "Study on subset size selection in digital image correlation for speckle patterns," *Opt. Exp.*, vol. 16, no. 10, pp. 7037–7148, 2008.

[33] B. Pan, Z. Lu, and H. Xie, "Mean intensity gradient: An effective global parameter for quality assessment of the speckle patterns used in digital image correlation," *Opt. Lasers Eng.*, vol. 48, no. 4, pp. 469–477, Apr. 2010.

[34] Y. Su, Q. Zhang, X. Xu, and Z. Gao, "Quality assessment of speckle patterns for DIC by consideration of both systematic errors and random errors," *Opt. Lasers Eng.*, vol. 86, pp. 132–142, Nov. 2016.

[35] X. Hu, Z. Xie, and F. Liu, "Assessment of speckle pattern quality in digital image correlation from the perspective of mean bias error," *Measurement*, vol. 173, Mar. 2021, Art. no. 108618.

[36] S. Yaofeng and J. H. L. Pang, "Study of optimal subset size in digital image correlation of speckle pattern images," *Opt. Lasers Eng.*, vol. 45, no. 9, pp. 967–974, Sep. 2007.

[37] X.-Y. Liu, R.-L. Li, H.-W. Zhao, T.-H. Cheng, G.-J. Cui, Q.-C. Tan, and G.-W. Meng, "Quality assessment of speckle patterns for digital image correlation by Shannon entropy," *Optik*, vol. 126, no. 23, pp. 4206–4211, Dec. 2015.

[38] D. J. Atkinson, M. van Rooyen, and T. H. Becker, "An artificial neural network for digital image correlation dynamic subset selection based on speckle pattern quality metrics," *Strain*, 2023, Art. no. e12471. [Online]. Available: https://onlinelibrary.wiley.com/action/showCitFormats?doi=10.1111%2Fstr.12471

[39] Y. Su and Q. Zhang, "Glare: A free and open-source software for generation and assessment of digital speckle pattern," *Opt. Lasers Eng.*, vol. 148, Jan. 2022, Art. no. 106766.

[40] S. Lan, Y. Gao, X. Xu, Y. Su, Y. Liu, C. Bai, S. Wu, and Q. Zhang, "Error analysis of surface-distribution and non-deformation of fluorescent beads for the IC-GN2 DVC algorithm," *Opt. Lasers Eng.*, vol. 140, May 2021, Art. no. 106541.

[41] Y. Barranger, P. Doumalin, J. C. Dupré, and A. Germaneau, "Digital image correlation accuracy: Influence of kind of speckle and recording setup," in *Proc. EPJ Web Conf.*, vol. 6, 2010, p. 31002.

[42] Y. Barranger, P. Doumalin, J. C. Dupré, and A. Germaneau, "Strain measurement by digital image correlation: Influence of two types of speckle patterns made from rigid or deformable marks," *Strain*, vol. 48, no. 5, pp. 357–365, Oct. 2012.

[43] Z. Jiang, "OpenCorr: An open source library for research and development of digital image correlation," *Opt. Lasers Eng.*, vol. 165, Jun. 2023, Art. no. 107566.

[44] H. Cui, Z. Zeng, H. Zhang, and F. Yang, "Reducing the systematic error of DIC using gradient filtering," *Measurement*, vol. 207, Feb. 2023, Art. no. 112366.

[45] X. Xu, Y. Su, Y. Cai, T. Cheng, and Q. Zhang, "Effects of various shape functions and subset size in local deformation measurements using DIC," *Experim. Mech.*, vol. 55, no. 8, pp. 1575–1590, Oct. 2015.

[46] B. Pan and B. Wang, "Digital image correlation with enhanced accuracy and efficiency: A comparison of two subpixel registration algorithms," *Experim. Mech.*, vol. 56, no. 8, pp. 1395–1409, Oct. 2016.

[47] W. Chen, Z. Jiang, L. Tang, Y. Liu, and Z. Liu, "Equal noise resistance of two mainstream iterative sub-pixel registration algorithms in digital image correlation," *Experim. Mech.*, vol. 57, no. 6, pp. 979–996, Jul. 2017.

[48] H. W. Schreier, "Systematic errors in digital image correlation caused by intensity interpolation," *Opt. Eng.*, vol. 39, no. 11, pp. 2915–2921, Nov. 2000.

[49] J. Baldoni, G. Lionello, F. Zama, and L. Cristofolini, "Comparison of different filtering strategies to reduce noise in strain measurement with digital image correlation," *J. Strain Anal. Eng. Des.*, vol. 51, no. 6, pp. 416–430, Aug. 2016.

[50] X. Zou, K. Li, and B. Pan, "The effect of low-pass pre-filtering on subvoxel registration algorithms in digital volume correlation: A revisited study," *Meas. Sci. Rev.*, vol. 20, no. 5, pp. 202–209, Oct. 2020.

[51] N. S. P. Kong, H. Ibrahim, and S. C. Hoo, "A literature review on histogram equalization and its variations for digital image enhancement," *Int. J. Innov., Manag. Technol.*, vol. 4, no. 4, p. 386, 2013.

[52] W. Zhang, S. Jin, P. Zhuang, Z. Liang, and C. Li, "Underwater image enhancement via piecewise color correction and dual prior optimized contrast enhancement," *IEEE Signal Process. Lett.*, vol. 30, pp. 229–233, 2023.

[53] W. Zhang, L. Zhou, P. Zhuang, G. Li, X. Pan, W. Zhao, and C. Li, "Underwater image enhancement via weighted wavelet visual perception fusion," *IEEE Trans. Circuits Syst. Video Technol.*, vol. 34, no. 4, pp. 2469–2483, Apr. 2024.

[54] A. Singh, S. Kushwaha, M. Alarfaj, and M. Singh, "Comprehensive overview of backpropagation algorithm for digital image denoising," *Electronics*, vol. 11, no. 10, p. 1590, May 2022.

[55] Y. Farooq and S. Savas, "Noise removal from the image using convolutional neural networks-based denoising auto encoder," *J. Emerg. Comput. Technol.*, vol. 3, no. 1, pp. 21–28, Mar. 2024.

[56] W. Yang, "Effect analysis of Fourier transform and neural network on image noise reduction," *Highlights Sci., Eng. Technol.*, vol. 88, pp. 64–71, Mar. 2024.

[57] Y. Q. Wang, M. A. Sutton, H. A. Bruck, and H. W. Schreier, "Quantitative error assessment in pattern matching: Effects of intensity pattern noise, interpolation, strain and image contrast on motion measurements," *Strain*, vol. 45, no. 2, pp. 160–178, Apr. 2009.

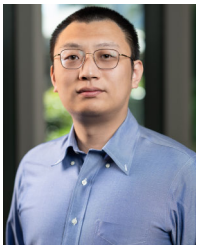

JIAQIU WANG was born in Xianyang, Shaanxi, China, in 1991. He received the B.Eng. degree from Chongqing University, Chongqing, China, in 2014, the M.Sc. (by Research) degree from the University of Dundee, Dundee, U.K., in 2016, and the Ph.D. degree from Queensland University of Technology, Brisbane, Australia, in 2020.

From 2020 to 2023, he was a Postdoctoral Researcher with Queensland University of Technology. From 2021 to 2022, he was a Facility Scientist with the Centre for Advanced Imaging, The University of Queensland, Brisbane. In 2023, he was appointed as a Senior Lecturer with the School of Engineering, London South Bank University, London, U.K. He has extensive experience in computational modeling and simulation, medical imaging and processing, and mechanical and fluidic experiments. His research interests include biomechanics and biomedical engineering.

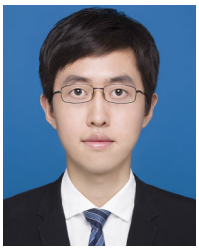

HAO WU was born in Xuzhou, Jiangsu, China, in 1994. He received the B.Eng. and M.Sc. degrees from Tianjin University, Tianjin, China, in 2017 and 2020, respectively. He is currently pursuing the Ph.D. degree with the School of Biological Science and Medical Engineering, Southeast University, China.

He has extensive experience in medical imaging and processing, mechanical experiments, and strain analysis. He has developed novel methods to analyze the strain by left atrium and arterial walls in relation to cardiovascular diseases. His current research interests include imaging-based strain computation method.

ZHENGDUO ZHU received the bachelor's degree majoring in game development and machine learning and computer vision from Monash University, and the master's degree majoring in game development and machine learning and computer vision from The Australian National University. He is currently pursuing the Ph.D. degree in computer science and biomedical with Queensland University of Technology. His research project is for the development of software that is able to provide biomechanical information on a specific blood vessel.

HUJIN XIE is a Postdoctoral Research Fellow with the Cardiovascular Research Group, Queensland University of Technology. His research interests include computational biomechanical simulation, medical image analysis, cardiovascular disease risk assessment, and medical digital twins.

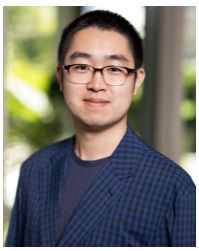

HAN YU received the Ph.D. degree in biomedical engineering from Queensland University of Technology, in 2022.

He started his research in cardiovascular biomechanics in 2016. His doctoral research focused on using cutting-edge ventricular mechanical simulation methods to predict outcomes of pulmonary valve replacement and evaluate novel surgical treatments by performing virtual surgeries for Tetralogy of Fallot patients. He is currently a Research Associate with Queensland University of Technology. His current work includes evaluating dementia and stroke risks of patients with Atrial Fibrillation.

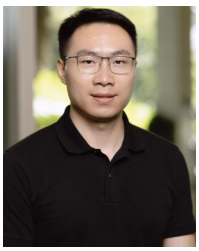

QIUXIANG HUANG is working on multidisciplinary research that crosses engineering and biology. He worked on developing fluid-structure interaction solvers for simulating collapsible blood vessels during his Ph.D. degree with the Flow Science Laboratory, University of New South Wales Canberra (UNSW Canberra). From 2021 to 2023, he continued his research career with UNSW Canberra as a Research Associate, working on understanding insect flight based on computational techniques. Currently, he is a Research Fellow with the Centre for Biomedical Technologies, Queensland University of Technology. He is interested in developing multi-scale coupling techniques for scientific and high-performance computing, including fluid-structure interactions with applications in blood flow, insect flight, and low-Reynolds turbulence.

YUQIAO XIANG was born in Chongqing, China. He received the B.Eng. degree from Chongqing University, in 2017, and the M.Sc. degree from The University of Queensland, in 2019. He is currently pursuing the Ph.D. degree with the School of Mechanical, Medical and Process Engineering, Queensland University of Technology, Australia. His current research interest includes imaging-based computational modeling in relation to cardiovascular diseases.

PHANI KUMARI PARITALA received the Ph.D. degree in biomedical engineering from Queensland University of Technology, Brisbane, QLD, in 2019. Her research interests include imaging-based computational modeling and stresses analysis in cardiovascular diseases.

JESSICA BENITEZ MENDIETA received the dual master's degrees in medical physics and lumbar spine biomechanics and the Ph.D. degree in cardiovascular biomechanics. She is a Biomedical Engineer. Her doctoral studies have provided her with extensive expertise in computational biomechanics, patient-specific medical imaging analysis, and experimental analysis of biological tissue. She also possesses a strong foundation in medical physics. Currently, her research focuses on analyzing the fluid and structural biomechanics of carotid arteries, coronary arteries, heart atrium, and intracranial aneurysms. She has developed novel methods to analyze the stresses experienced by plaque components and arterial walls.

HAVEENA ANBANANTHAN received the Bachelor of Engineering degree (Hons.) in medical engineering from Queensland University of Technology (QUT), in 2020, where she is currently pursuing the Ph.D. degree, specializing in the modeling and simulation of cardiovascular diseases. Her current research is centered on understanding intracranial aneurysms hemodynamics and vessel wall mechanics using computational fluid dynamics (CFD) and fluid-structure interaction (FSI) simulations. To support her findings, she fabricates 3-D-printed models of aneurysms and uses particle image velocimetry (PIV) imaging to visualize flow patterns within the model.

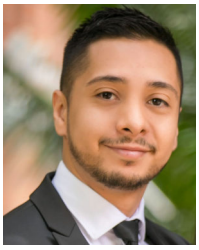

JORGE ALBERTO AMAYA CATANO was born in Medellin, Colombia. He received the degree in mechanical engineering from EAFIT University, Medellin, Colombia, and the master's degree in engineering from EAFIT University, in 2014. He is currently pursuing the Ph.D. degree in biomedical engineering with Queensland University of Technology, specializing in cardiovascular and tissue engineering. Within this academic context, he cultivated expertise across various topics, encompassing fluid dynamics, biomaterials, bioreactor development, 3-D printing, bio-fabrication, and cell culture techniques.

Demonstrating leadership and collaboration, he's excelled in prominent companies, spanning manufacturing, production, design, and equipment installation. Moreover, he has made notable contributions in academia as a tutor and a research assistant within his field. His career transitioned into biomedical engineering, where he was a design engineer with medical devices research company. In this role, he played a pivotal part in developing an implantable heart failure device.

RUNXIN FANG received the Ph.D. degree in biomedical engineering from the Biomedical Engineering School, Southeast University, Nanjing, China. He specializes in the cardiovascular hemodynamics. His research work encompasses computational modeling of vascular systems based on patient-specific medical imaging. With an interdisciplinary approach, combining theoretical simulation, biological experiments, and mechanical measurements, he conducts comprehensive models, in vivo, and ex vivo experiments to explore the fundamental biomechanical mechanisms and biophysical laws underlying the development of cardiovascular diseases.

LUPING WANG was born in Hangzhou, Zhejiang, China. She received the B.Eng., M.Sc., and Ph.D. degrees in biomedical engineering from Southeast University, Nanjing, China, in 2011, 2014, and 2023, respectively. In 2023, she was appointed as a Lecturer with the College of Mechanical and Electrical Engineering, China Jiliang University, Hangzhou. She has skills and experience in computational modeling, finite element analysis, and mechanical experiments. Her research interests include biomechanics and biomedical engineering.

ZHIYONG LI received the B.Eng. degree in civil engineering from Tongji University, in 1998, the Ph.D. degree in biomedical engineering from Queen Mary University of London, in 2004, and the M.A. degree from the University of Cambridge, in 2009.

He is a Professor in biomedical engineering with Queensland University of Technology (QUT). He was a Research Fellow and a Senior Research Fellow with the University of Cambridge, from 2004 to 2010. He was an Elected Fellow of Wolfson College. His main research field is biomechanics and mechanobiology, with a long-term research interest in cardiovascular diseases (atherosclerosis, aneurysm, and atrial affiliation). The main focus of his work has been the development of novel technologies for detection of high-risk rupture-prone plaques in patients with carotid and coronary atherosclerosis. The work involves MRI/IVUS/OCT imaging, stress analysis, material characterization, mathematical/computational modelling and numerical methods. He has made significant contributions to understanding the biomechanics of plaque rupture.

Prof. Li received the ARC Future Fellowship, in 2014; and the 2015 Australia Vascular Biology Society Achievement and Career Development Award.